PHYSICAL REVIEW B **98**, 165303 (2018)

Quasilocal plasmons in the insulator-metal transition in the Mott-type perovskites $Eu_{0.3}Ba_{0.7}Ti_{1-x}Nb_xO_3$

A. Chaudhuri,[1,2,*] K. Rubi,[3] T. C. Asmara,[1,2] X. Chi,[2,3] X. J. Yu,[2] R. Mahendiran,[2,3,†] and A. Rusydi[1,2,3,4,‡]
[1] *NUSSNI-NanoCore, National University of Singapore, Singapore 117576, Singapore*
[2] *Singapore Synchrotron Light Source, National University of Singapore, 5 Research Link, Singapore 117603, Singapore*
[3] *Department of Physics, National University of Singapore, Singapore 117542, Singapore*
[4] *National University of Singapore Graduate School for Integrative Sciences and Engineering (NGS), 28 Medical Drive, Singapore 117456, Singapore*

(Received 5 February 2018; revised manuscript received 30 August 2018; published 5 October 2018)

Tunable plasmons in the infrared energy range are of critical importance in designing novel plasmonic materials with fascinating uses in various solid-state applications, such as plasmonics, transformation optics, and biochemical sensors. Perovskite oxides are promising building-block materials for plasmon generation because they have wide and tunable band gaps as well as the possibility of having low plasmonic loss. Here, using a combination of high-resolution spectroscopic ellipsometry, x-ray-absorption spectroscopy both at Ti $L_{3,2}$ and O K edges, and transport measurements, we report a highly tunable quasilocal plasmon at room temperature in the long-wavelength infrared range (<1 eV) in a Mott-type insulator $Eu_{0.30}Ba_{0.70}Ti_{(1-x)}Nb_xO_3$ ($0 \leqslant x \leqslant 0.10$). Interestingly, the quasilocal plasmon, which can be controlled by varying Nb substitution, is originated by the effect of screening of Eu $4f$ electrons accompanied by band modulation that alters the relative strength of charge-transfer and Mott-transition interactions, yielding an insulator-metal transition. These quasilocal plasmons in Mott-type perovskites may open a strategy for device fabrication in the infrared-to-visible region.

DOI: 10.1103/PhysRevB.98.165303

I. INTRODUCTION

The conventional plasmon is a fundamental phenomenon of collective oscillations of delocalized (or free) electrons in response to electromagnetic excitations and commonly occurs in metals in the visible to UV range [1]. The recent research trend in plasmonics highlights the importance of plasmon applications in the IR region [2–5] as plasmons in this energy range are capable of, for example, sensing biochemical environment [3,6–8], leading to the successful designing of novel medical devices [9] as well as use in solar energy harvesting [10–13], transformation optics [14–16], and much more [17]. In terms of complex dielectric functions, the conventional plasmonic materials are composed of metallic components with high loss, and, hence, are not ideal for designing devices in this energy realm [18]. To overcome this shortcoming, recent research focus has broadened to search for "metal-like materials." As alternative plasmonic materials, semiconductor-based oxide materials or transparent oxides are promising candidates as they offer low intrinsic loss and tunability in the near-IR region [19]. However, the choices of such oxides in plasmonics applications are limited.

Here, we observe a quasilocal plasmon at room temperature in a perovskite oxide group called $Eu_{0.30}Ba_{0.70}Ti_{(1-x)}Nb_xO_3$ ($0 \leqslant x \leqslant 0.10$) prepared by replacing 30% Ba^{2+} with isovalent Eu^{2+} in the A site of $BaTiO_3$ (BTO). Interestingly, it shows an insulator-metal transition (IMT) at 10% Nb substitution with an increase in the electrical conductivity by several orders of magnitude [20]. Here we report simultaneous occurrences of both plasmon formation and IMT transition in $Eu_{0.30}Ba_{0.70}Ti_{(1-x)}Nb_xO_3$. The electronic and optical properties of Nb-substituted EBTOs, viz., $Eu_{0.30}Ba_{0.7}TiO_3$ (EBTO), $Eu_{0.30}Ba_{0.70}Ti_{0.95}Nb_{0.05}O_3$ (EBTO-5Nb), and $Eu_{0.30}Ba_{0.70}Ti_{0.90}Nb_{0.10}O_3$ (EBTO-10Nb), are studied using high-resolution spectroscopic ellipsometry (SE), x-ray-absorption spectroscopy (XAS) at Ti $L_{3,2}$ and O K edges, x-ray photoelectron spectroscopy (XPS), and transport measurements.

Our paper reveals that EBTO is a Mott-type insulator with dielectric properties that change significantly with the Nb substitutions. As the Nb substitutions become higher, the hybridization between the O $2p$ and the metal cations (especially Eu^{2+}) is significantly modified, and the charge-transfer (CT) process from O $2p$ to d band becomes stronger at the expense of Mott transitions which become weaker and eventually cease to exist in the metallic EBTO-10Nb. As a combined result of the weak Eu-O hybridizations and the associated screening effect, a systematic increase of partly delocalized electrons is manifested in the form of a (Nb) substitution-controlled quasilocal plasmon in the infrared region. The associated electronic band modulation, which is impacted by the onsite screening effect, is responsible also for the insulator-metal transitions in the EBTO-10Nb.

---

[*] Corresponding author: nniac@nus.edu.sg
[†] Correspondence to: phyrm@nus.edu.sg
[‡] Correspondence to: phyandri@nus.edu.sg

II. EXPERIMENTAL

A. Materials preparations and structural characterizations

$Eu_{0.30}Ba_{0.70}Ti_{1-x}Nb_xO_3$ ($x = 0.00$, 0.05, and 0.10) polycrystalline samples are synthesized using conventional solid-state reaction method. The stoichiometric amount of $BaCoO_3$, Eu_2O_3, and TiO_2 and Nb_2O_5 powders was mixed, grounded, and annealed at 1200 °C for 24 h in reduced atmosphere (95% Ar and 5% H_2) for reducing Eu^{3+} into Eu^{2+}. After two consecutive grinding and annealing sessions, the powder was pressed into a pellet and then sintered at 1300 °C for 24 h in the same atmosphere. A Philips X'PERT MPD powder x-ray diffractometer was employed for structure characterization at room temperature using CuKα radiation. All samples are in single phase and crystallized in cubic perovskite structure with space group Pm-$3m$ and lattice constant $a = 3.9746$, 3.9825, and 3.9851 Å for $x = 0.00$, 0.05, and 0.10, respectively.

B. Transport measurement

The electrical resistance (R) is measured using the thermal transport option in the Physical Property Measurement System, Quantum Design, USA.

C. Spectroscopic ellipsometry

Spectroscopic ellipsometric parameters Ψ and Δ (viz., the ratio of the amplitude and phase difference between p- and s-polarized reflected light, respectively) are collected at 65, 70, and 75° angles of incidence, with a photon energy range between 0.4 and 5.0 eV using a Woollam V-vase ellipsometer. Details of the instrument and the measurement geometry are described elsewhere [21]. The real and imaginary parts of the dielectric constant (ε_1 and ε_2) are extracted using a least-squares regression analysis and an unweighted root-mean-square error function by fitting the experimental spectra with Woollam Complete Ease software. The parameters correspond to the surface roughness of the EBTO, EBTO-5Nb, and EBTO-10Nb samples and a parametrization of the respective dielectric functions are evaluated by a combination of Herzinger-Johs PSemi-Tri oscillator functions. The optical properties of the surface roughness layer are estimated by a Bruggeman effective medium approximation consisting of a 50% bulk film and 50% void mixture.

The following equations are used to evaluate the dielectric properties for the current set of perovskites.

(1) Complex dielectric function $\varepsilon(\omega) = \varepsilon_1(\omega) + i\varepsilon_2(\omega)$ (ω = angular frequency of the incident photon).

(2) Optical conductivity $\sigma_1(\omega) = \varepsilon_0\varepsilon_2(\omega)\omega$ (ε_0 is the free-space permittivity).

(3) Loss-function $-\mathrm{Im}\,[\varepsilon^{-1}(\omega)] = \frac{\varepsilon_2(\omega)}{[\varepsilon_1^2(\omega)+\varepsilon_2^2(\omega)]}$.

(4) Refractive index $n(\omega) = \sqrt{\frac{1}{2}[\sqrt{\varepsilon_1^2(\omega)+\varepsilon_2^2(\omega)}+\varepsilon_1(\omega)]}$.

(5) Extinction coefficient $\kappa(\omega) = \sqrt{\frac{1}{2}[\sqrt{\varepsilon_1^2(\omega)+\varepsilon_2^2(\omega)}-\varepsilon_1(\omega)]}$.

(6) Normal incident reflectivity $R(\omega) = \frac{[n(\omega)-1]^2+\kappa^2(\omega)}{[n(\omega)+1]^2+\kappa^2(\omega)}$.

(7) Absorption coefficient $\alpha(\omega) = 4\pi\kappa(\omega)/\lambda$ (λ is the photon wavelength).

D. XAS and XPS

The soft x-ray-absorption spectra (XAS) are collected for these samples at the Surface, Interface and Nanostructure Science (SINS) beamline of the Singapore Synchrotron Light Source (SSLS) synchrotron facility, National University of Singapore. Details of the beamline are described elsewhere [22]. The XAS spectra (Ti L edge and O K edge) are obtained in the total electron yield mode by registering the current drained to the ground from the sample. The spectra are normalized by the incident photon flux.

The XPS spectra are recorded using an electron spectroscopy for chemical analysis (ESCA) on an Omicron EA125 U7 hemispherical electron spectrometer with monochromatized Mg Kα radiation ($h\nu = 1253$ eV). The base pressure is maintained below 10^{-9} mbar during measurements. All spectra are collected at room temperature and calibrated against the Au $4f_{7/2}$ signal from an Au foil (84.0 eV).

III. RESULTS

A. Electrical conductivity

Figure 1 shows the temperature profile of electrical conductivity (σ) of EBTO-5Nb and EBTO-10Nb, estimated from the measured resistivity of the corresponding Nb substituted EBTOs. The electrical resistivity of the parent compound, EBTO ($x = 0$), is significantly high to be detected. The temperature profile of the conductivity curve indicates that IMT occurs for EBTO-10Nb, while for ENTO-5Nb the referred curve shows those of insulators.

B. Dielectric properties and the plasmonic excitation

Experimental Ψ and Δ for EBTO, EBTO-5Nb, and EBTO-10Nb are shown in Fig. 2 together with the fittings from their analysis. To substantiate the formation of the quasilocal plasmonic excitation, we show, in Fig. 3, the loss function, reflectivity R, and the real part ε_1 and imaginary part ε_2 of the complex dielectric functions derived using the spectroscopic ellipsometry data for the three samples, viz., EBTO, EBTO-5Nb, and EBTO-10Nb collected at room temperature in the optical energy range of 0.4–5.0 eV.

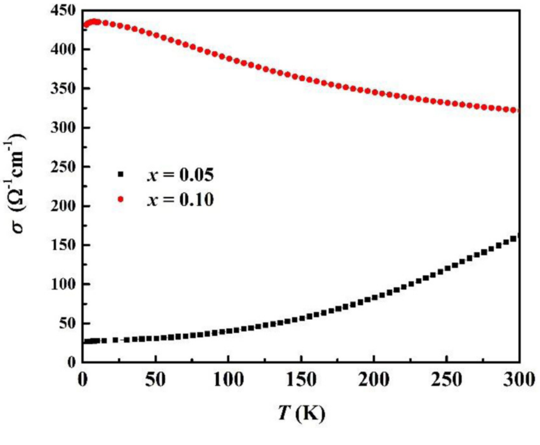

FIG. 1. Temperature dependence of electrical conductivity (σ) for $Eu_{0.30}Ba_{0.70}Ti_{1-x}Nb_xO_3$ for $x = 0.05$ (EBTO-5Nb) and $x = 0.10$ (EBTO-10Nb).

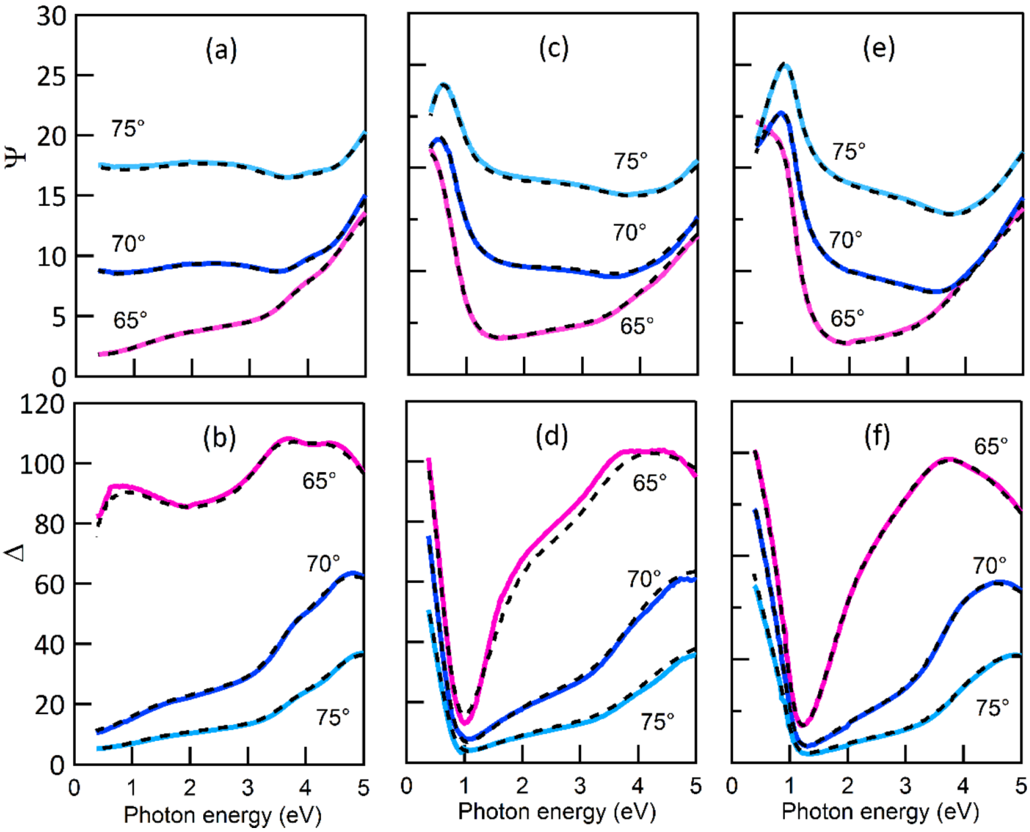

FIG. 2. Experimental (solid curves) and fitted (dotted curves) data of Ψ and Δ for EBTO (a, b), EBTO-5Nb (c, d), and EBTO-10Nb (e, f) obtained at 65, 70, and 75°.

The loss function of EBTO-5Nb and EBTO-10Nb shows distinct peaks, respectively, at 0.56 and 0.86 eV in Fig. 3(a) associated also with the reflectivity edges below 1 eV in Fig. 3(b) clearly indicating plasmonic excitation in the IR energy range in the Nb-substituted EBTOs. The Nb substitution systematically increases the energy and the strength (amplitude) of the plasmonic excitations with several unusual properties discussed below.

First, the strong optical transitions in Fig. 3(d) in EBTO-5Nb and EBTO-10Nb below 1 eV, associated with their plasmonic excitations, are not originated from the conventional (bulk) plasmon excitations. This is confirmed by the real part of the complex dielectric function [Fig. 3(c)] showing non-negative minima (for example, the ε_1 minima at 0.56 eV for EBTO-10Nb). It has been well established that ε_1 for the conventional plasmon undergoes a crossover at the screened plasma frequency, from positive to negative values giving a measure of delocalization of the electrons [23]. From this point of view, the electrons participating in the plasmonic excitations in the Nb-substituted EBTOs are quasilocal in nature. It will be later shown that the plasmonic oscillation is likely to be a combined contribution from the localized f electrons (Eu $4f$) and d^1 electrons, all being close to the Fermi level.

Second, the loss-function peaks, shown in Fig. 3(a), appear to be significantly away (>0.5 eV) from the low-energy transitions (the tail of which is observed and denoted by A) in the ε_2 profiles of EBTO-5Nb and EBTO-10Nb given in Fig. 3(d). Such energy mismatch between the loss-function peaks and the referred low-energy transitions below 1 eV suppresses the plasmonic loss. In other words, the quasilocal plasmonic excitations in the Nb-substituted EBTOs are weakly coupled with the optical excitation. However, we do not rule out coupling of plasmonic excitations with other excitations including, for example, the polaronic excitations in the far-IR range reported in the Nb-doped perovskite oxides [24]. Such coupling may enhance the transition strengths observed in the Nb-substituted EBTOs in which the low-energy transitions appear to be stronger than the transitions at D, as one can find in Fig. 3(d) identified as the charge-transfer excitations that are usually the strongest interband transitions in perovskites.

C. Interband transitions

To understand the source and the mechanism that forms this special type of plasmonic excitations in the Nb-substituted EBTOs, we next identify and characterize the transitions B–D shown in Fig. 3(d). The transitions at B in EBTO and B′ in EBTO-5Nb are Mott transitions, typically observed for the localized partially filled d electrons in the Mott-Hubbard type insulator [25]. We have established using XAS and XPS study (see Sec. IIIE) that both the Ti and Nb at the B site have d^1 electronic structures in the Nb-substituted EBTOs. The interband transitions covering the peaks around C (~4.2) eV and D (~5 eV) arise due to the CT process of O $2p$ to d states of the transition metals, as observed in the conventional Ti based perovskite structures [26,27].

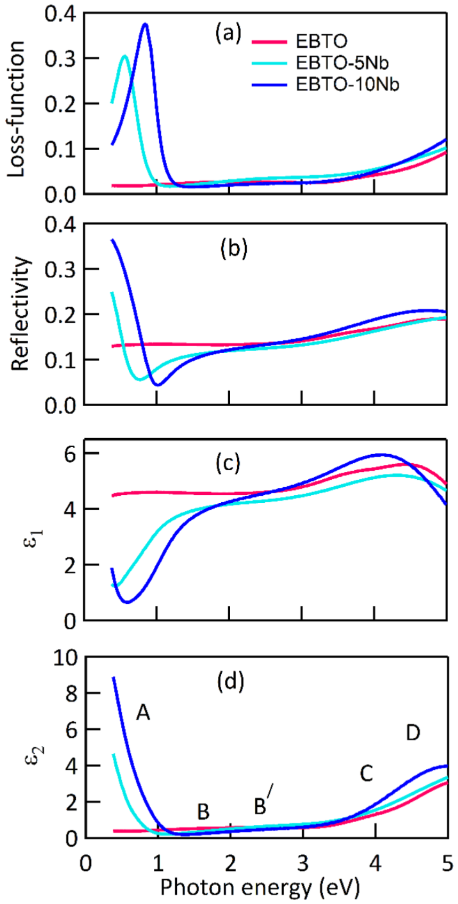

FIG. 3. (a) Loss function**,** (b) reflectivity R, (c) real part (ε_1) of the dielectric function**,** and **(**d**)** imaginary part (ε_2) of the dielectric function for EBTO (magenta), EBTO-5Nb (light blue), and EBTO-10Nb (dark blue).

D. Spectral weight transfer

Since we are able to identify the optical transitions in the three EBTOs, we can quantify the change in the optical transitions associated individually with the quasilocal plasmon, Mott transition, and charge transfer. This change may be established quantitatively using the optical conductivity spectra $\sigma_1(\omega)$ of the EBTOs because $\sigma_1(\omega)$ satisfies the f-sum (charge conservation) rule and is related to the total electron density n by the relation $\int_0^\infty \sigma_1(\omega)\, d\omega = \pi n e^2/2m_e$, where m_e is the rest mass of the electron [28]. For a finite-energy range, the integral can be expressed as $W = \int_{E_1}^{E_2} \sigma_1(E) dE$. W is termed as the spectral weight transfer (SWT) and is proportional to the *effective* number of electrons participating in the optical transitions within the energy range $[E_1,\ E_2]$. Considering the experimental energy range from 0.4 to 5.0 eV of our observed spectra, we divide the SWT into three different ranges, viz., W_1 for energy range 0.4−1.0 eV (quasilocal plasmon range), W_2 for 1.0−3.5 eV (Mott-transition range), and W_3 for 3.5−5.0 eV (charge-transfer range). Estimated W_1, W_2, and W_3 and their sum W for each of the perovskites have been shown in Fig. 4 (inset).

We see in Fig. 4 that W_1 and W_3 increase considerably with Nb incorporation whereas W_2 decreases, indicating clearly that the electron participates in the plasmonic response and the CT process increases whereas that in the Mott transition decreases by Nb substitution in these EBTOs. A smaller number of electron transitions across the Mott gap is consistent with the widening Mott gap E_g in EBTO-5Nb and EBTO-10Nb. Despite a systematically weaker contribution of Mott electrons, one can notice from Fig. 4 (inset) that the total effective number of electrons (W) increases with Nb substitution, indicating an increase in the electron population in the conduction band. This increase is mainly due to a stronger CT process (W_3) in the Nb-substituted EBTOs in comparison to the parent one. The increase in W, as noticed for each of the three perovskites, estimated over the limited energy range of 0.4–5.0 eV is an indication that the electronic transition must extend beyond the selected energy range to satisfy the charge conservation, which is typical of highly correlated systems.

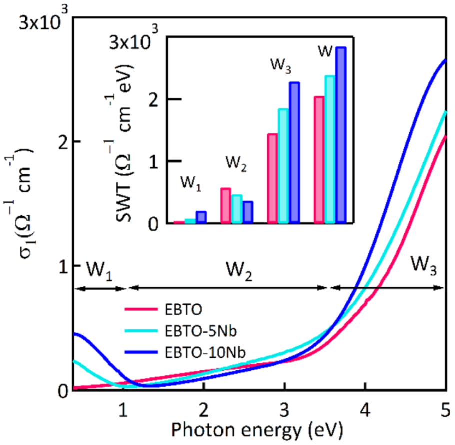

FIG. 4. Optical conductivity (σ_1) spectra and spectral weight of EBTO, EBTO-5Nb, and EBTO-10Nb. Inset: The estimated SWT over three energy ranges: 0.4–1.0 eV (W_1), 1.0–3.5 eV (W_2), and 3.5–5.0 eV (W_3). $W = W_1 + W_2 + W_3$.

E. XAS and XPS spectra

Figure 5 shows the XAS spectra near the Ti $L_{3,2}$ edge for the selected compositions EBTO, EBTO-5Nb, and EBTO-10Nb. An octahedral ligand field causes the Ti L_3 and L_2 absorption peaks to split into subpeaks t_{2g} (labeled as L_3t_{2g} and L_2t_{2g}) and e_g (labeled as L_3e_g and L_2e_g), as shown in Fig. 5.

The characteristic features of the Ti $L_{3,2}$ edge XAS spectrum, measured in the $Ba_{0.7}Eu_{0.3}TiO_3$ sample (EBTO), are in good agreement with that of the Ti^{4+} state [29] implying that the parent compound (EBTO) is mainly dominated by Ti^{4+} valence states. The peak at 458 eV, which is a characteristic of the Ti^{3+} state [30], gradually increases (Fig. 5), indicating a clear formation of Ti^{3+} ions with Nb incorporation. The satellite structure of EBTO around 469 eV (nearly 13 eV above the absorption edge) is also modified considerably with Nb substitution, confirming that the hybridization between the Ti $3d$ and O $2p$ electrons becomes weaker with Ti^{3+} formation [31].

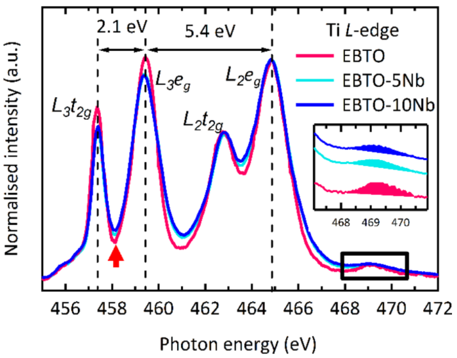

FIG. 5. XAS spectra of the Ti $L_{3,2}$ edge**.** The spectra are normalized to the $L_2\,e_g$ edge for the compounds EBTO, EBTO-5Nb, and EBTO-10Nb. XAS peak position energy ~458 eV, marked by the red arrow, is indicating the increase of Ti^{3+} with Nb substitution. Satellite peaks within 467–471 eV (highlighted by the box) are enlarged (inset). The shaded area indicates hybridization strength.

The core-level XPS spectrum from the Nb $3d$ region confirms the presence of Nb^{4+} oxidation states [32] in EBTO-5Nb and EBTO-10Nb as shown in Fig. 6. Since the EBTO is substituted with Nb^{5+}, the Nb ions have undergone $4d^0 \rightarrow 4d^1$ change contributing d electrons, akin to the other B-site cation Ti^{3+} ($3d^1$) in the conduction band.

To estimate the change in hybridization between the cation and the anion orbitals and their impact on electronic structure, we show the O K-edge XAS spectra for the three EBTOs in Fig. 7, plotted also with the reported density of states of some selected electronic orbitals of the metal ions for reference [33–35]. Drop in the intensity for peak X_1 (~530 eV) with concurrent increase in the intensity in X_4 and X_5 regions confirms the Ti^{3+} formation [36]. Since the peak X_1 is originated by the transition from the O $1s$ level to the hybridized O $2p$-Ti $3d$ (Ti t_{2g}) level, the decrease in the intensity of the peak implies a weaker O $2p$-Ti $3d$ (Ti t_{2g}) hybridization [37] in comparison to that in the parent EBTO, thus complementing the observation made in the Ti t_{2g} and the satellite peak in the Ti L edge in the XAS.

Another significant modification is observed in Fig. 7 for the energy range 531–535 eV covering X_2 and X_3 peak areas of the O K edge in EBTO-5Nb in comparison to that of EBTO. This energy range is mainly contributed by Ti $3d$ (Ti e_g), Nb $4d$ (Nb e_g), and Eu $4f$ antibonding states [33,38,39] which are hybridized with O $2p$. A qualitative comparison between the O K edges obtained from Nb-doped BTO [38] and the EBTO-5Nb enables us to claim that the distinct decrease in the intensity of the X_2-X_3 peak area is due to the change in the hybridization (covalency) between the O $2p$ and the Eu. The p-f hybridization between O^{2-} and Eu^{2+} in EBTO is likely to be weakened significantly in EBTO-5Nb. Further Nb substitution (for example, EBTO-10Nb) enhances O^{2-} hybridization with cation (Ba) orbitals in the higher-energy states (the X_4-X_5 region and beyond) at the cost of the hybridization with the lower-energy states covering X_2-X_3.

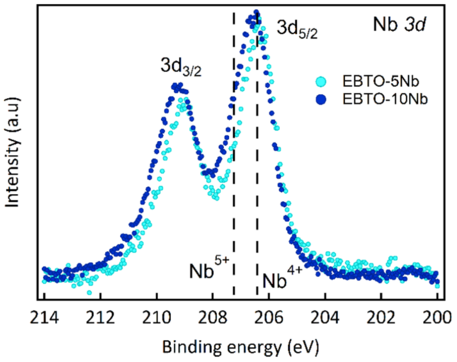

FIG. 6. XPS of Nb $3d$ collected from EBTO-5Nb and EBTO-10Nb.

F. Band-structure scheme

To understand the electronic (band) modulation and the associated electronic transitions, as shown in Fig. 3(d), giving the quasilocal plasmon and the IMT for the EBTOs studied here, we consider the Mott-Hubbard model, typical for such type of strongly correlated systems. The occupied d band, contributed by Ti $3d^1$ and Nb $4d^1$, splits into upper Hubbard band (UHB) and lower Hubbard band by the onsite Coulomb repulsion (U) of the d electrons according to the Hubbard model, where the width of the Hubbard band W is related to U as $U \sim E_g + W$. We determine the Mott gap energies (E_g) for EBTO, EBTO-5Nb, and EBTO-10Nb from the optical conductivity profiles. The optical conductivity curve just above the quasilocal plasmon energy range has been linearly fitted and the fitting line is extrapolated onto the energy axis to determine the corresponding Mott gap as shown by the dotted lines in Fig. 8. E_g values increase with Nb substitution: E_{g_1}(0.40 eV for EBTO) $<$ E_{g_2} (1.17 eV for EBTO-5Nb) $<$ E_{g_3} (1.32 eV for EBTO-10Nb). To estimate W, we assume transition B (~1.80 eV) and B′ (~2.45 eV) to be the Mott-transition peak scaled to U in a first approximation. The estimated W is ~1.4 eV for both cases in both EBTO and EBTO-5Nb; we retain this W for the EBTO-10Nb too.

Figure 9 shows probable band schemes, where Eu $4f$ bands in EBTO and EBTO-5Nb are positioned 0.8 eV below the lowest conduction band (in this case the bottom of the UHB). This positioning of the Eu $4f$ is based on an assumption that the Eu $4f$ band dissects the gap between the highest occupied O $2p$ and the lowest unoccupied d state (this gap is essentially the onset energy for the charge-transfer process) in 1:3 ratio, as noticed from a recent report on $\mathrm{EuTiO_3}$ [39]. This approximation for Eu $4f$ band position (i.e., 0.8 eV below the unoccupied lowest d state) is consistent with <1 eV gap between Eu $4f$ and Ti $3d$ in another recent calculation for $\mathrm{Eu_{50}Ba_{50}TiO_3}$ [33].

Based on SE and XAS results together with a previous result on Nb-doped $\mathrm{SrTiO_3}$ [24], one may suggest that, at *room temperature*, new midgap states are formed upon Nb substitution following the Hubbard model of insulator-metal transition [40]. These are illustrated in Figs. 9(b) and 9(c). Considering the fact that the system is not a regular metal, we propose two midgap states: one in the occupied and another in the unoccupied state with a very small finite gap in between. From a detail observation of the band structure, we imply that the unoccupied midgap state is likely to be formed by the higher-energy unoccupied Ti t_{2g} states, which populate the bottom of

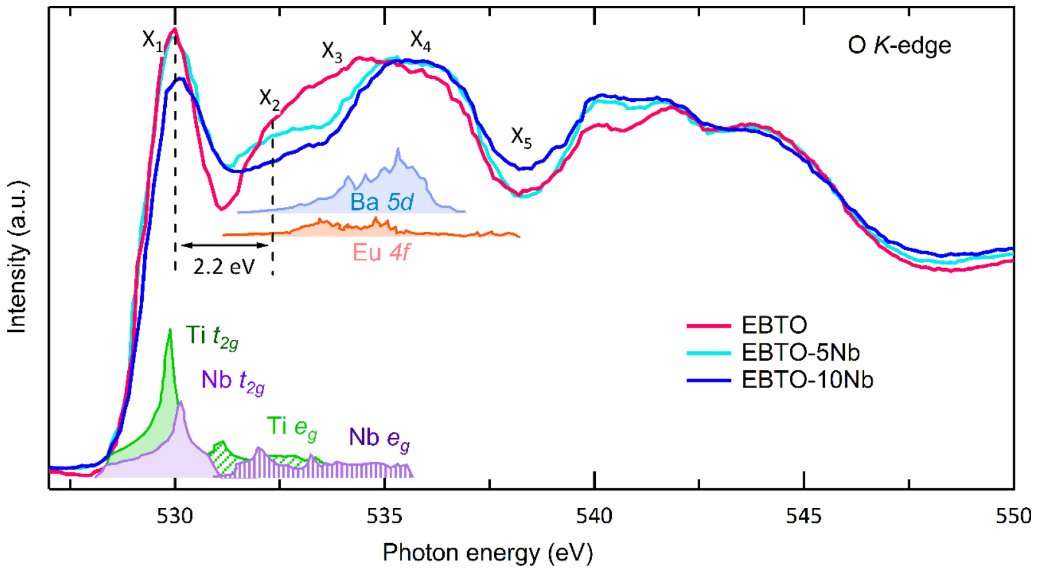

FIG. 7. O *K*-edge XAS spectra collected from EBTO, EBTO-5Nb, and EBTO-10Nb. Reported DOS for some selected cation orbitals are shown in the figure.

the UHB. The proposed band structure also suggests that, with Nb substitution, charge-transfer transition tends to dominate the Mott transitions, which is quantitatively confirmed by the estimated spectral weight transfer, discussed in Sec. IIID.

IV. DISCUSSION

By combining our experimental data and the band modulation scheme, we now discuss the origin of the quasilocal plasmon and the role of electrons in Nb $4d$ (forming the outer shell among the d states) and Eu $4f$ orbitals. To understand the contribution of Eu $4f$ in the plasmon formation in the Nb-substituted EBTOs, we compare the loss functions of Nb-substituted EBTOs with the available data of Nb-doped SrTiO$_3$ (STO), taken as a prototype of a non-Eu-based titanate. We calculate loss function spectra of Nb-doped STO from ε_2 (derived from the optical conductivity spectra [24]) and ε_1 [41] to estimate the free-electron concentration, shown in Fig. 10(a). In case of Nb-doped STO, a peak observed in loss function is accompanied by a negative value of ε_1, which is a signature of conventional plasmon formation by free electrons. We calculate plasmon energy (E_p) for these STOs as a function of Nb doping, by assuming that the d^1 electrons are to be fully free, using the known free-electron gas relation, $E_p^2 = \hbar^2 \frac{ne^2}{m\varepsilon_0}$, where n is the concentration of the d^1 electrons, e is charge of the electron, m is rest mass of the electron, and ε_0 is permittivity of free space. We then plot E_p versus $\sqrt{n}$ as shown in Fig. 10(b). The observed and calculated values of E_p for EBTO-5Nb and EBTO-10Nb are also included in the referred figure for comparison.

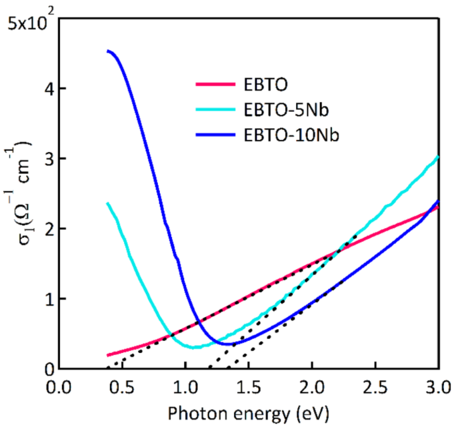

FIG. 8. Determination of Mott gap (E_g) by extrapolating the optical conductivity (σ_1) on the energy axis (x axis). The estimated Mott gaps for EBTO, EBTO-5Nb, and EBTO-10Nb are, respectively, 0.40, 1.17, and 1.32 eV. Optical conductivity data have been shown up to the energy range 0–3 eV for clarity.

As one can notice in Fig. 10(b), the observed E_p values are lower than the calculated E_p indicating that the effective number of d^1 electrons participating in plasmon oscillation is less than the total number of Nb $4d^1$ electrons for corresponding Nb substitution. In fact, an estimation from Fig. 10(b) suggests that only 10–20% of the Nb $4d^1$ electrons may be able to give the plasmon oscillations in Nb-doped STOs. Assuming identical contributions of Nb $4d^1$ electrons, the predicted E_p values in EBTO-5Nb and EBTO-10Nb would be, respectively, 0.4 and 0.6 eV. However, our observation (~0.5 and ~0.8 eV) clearly suggests a different quantitative contribution of Nb $4d^1$ electrons to form the plasmon peaks in Nb substituted EBTOs, which further indicates that Eu $4f$ electrons contribute in the unconventional plasmon formation in Nb substituted EBTO. Moreover, the ε_1 profile in our paper, corresponding to the plasmon oscillation, does not show zero crossing irrespective of Mott insulator (EBTO-5Nb) or metal (EBTO-10Nb), which is a clear indication that the electrons participating in plasmonic oscillation are loosely bound or quasilocal instead of free electrons as observed for Nb doped STOs.

Considering the band modulations in Nb-substituted EBTOs given in Fig. 9, Eu $4f$ is close to the Fermi energy. We argue that the source of the higher electron concentration, as discussed above, is controlled by the f-d hybridization (be-

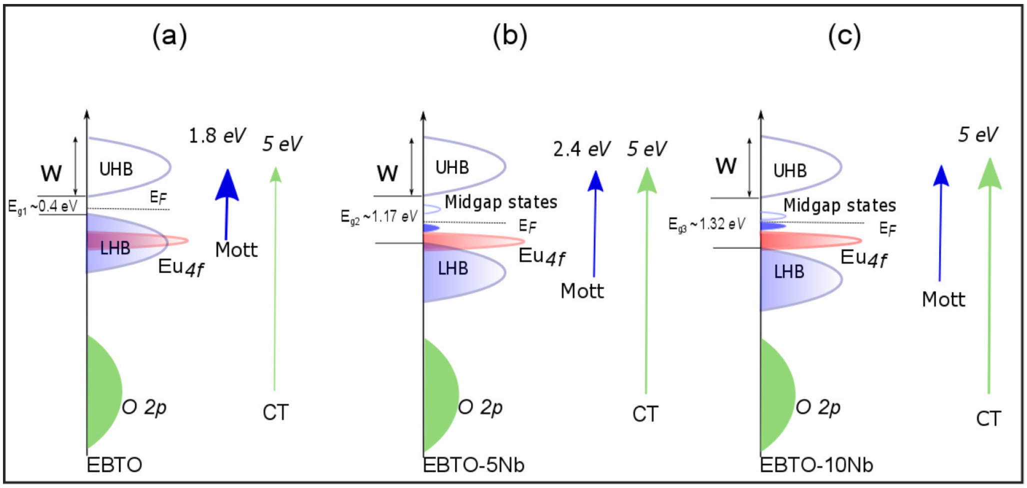

FIG. 9. Possible band-structure scheme in (a) EBTO, (b) EBTO-5Nb, and (c) EBTO-10Nb. Hubbard interaction $U \sim E_g + W$. E_{g1}, E_{g2}, and E_{g3} are the Mott gaps (in eV) for EBTO, EBTO-5Nb, and EBTO-10Nb, respectively; W is Hubbard bandwidth. E_F denotes Fermi level. The occupied (solid) and unoccupied (empty) midgap states are shown for EBTO-5Nb and EBTO-10Nb. Thickness of arrows qualitatively indicates strength of the transitions.

tween localized Eu $4f$ and d electrons). The f-d hybridization to form such orbital mixing has already been reported in ETO [35]. The enhanced d electron concentration associated with the Nb substitution controls the electron population and tunes the narrow gap between the occupied and unoccupied midgap states. Based on our measured conductivity versus temperature profile as shown in Fig. 1, we conclude, for EBTO-5Nb, the occupied and unoccupied midgap states have relatively wide separation and, hence, show the insulating nature, while the referred midgap states tend to merge in the proximity of Fermi level showing the metallic character, as we observe in the case of EBTO-10Nb. The plasmon oscillation originated by these midgap-state electrons retains the quasilocal nature (and an associated nonzero ε_1) as long as the f-d hybridization exists between the participating electrons irrespective of their affiliations: they may belong to a nonmetallic or a metallic material as we observe, respectively, for EBTO-5Nb and EBTO-10Nb.

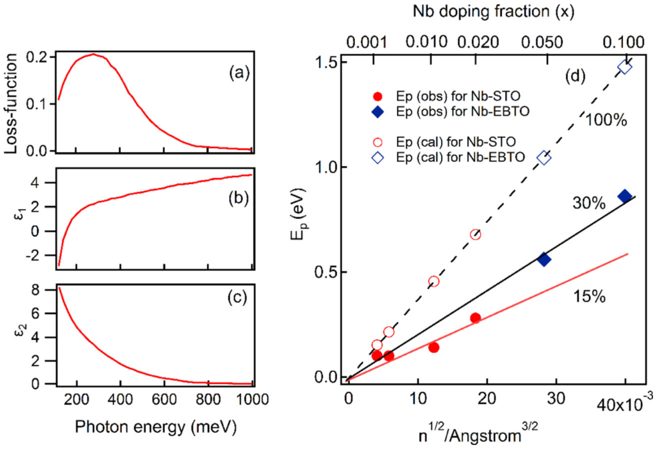

FIG. 10. Dielectric functions of $SrTi_{(1-x)}Nb_xO_3$ ($x = 0.02$), generated from Refs. [24,41] at room temperature for photon energies between 100 and 1000 meV: (a) loss function, (b) real part ε_1, and (c) imaginary part ε_2 of the complex dielectric function. (d) Comparison of E_p as a function of $\sqrt{n}$ for $SrTi_{(1-x)}Nb_xO_3$ ($x = 0.00, 0.002, 0.009, 0.02$) and $Eu_{0.30}Ba_{0.70}Ti_{(1-x)}Nb_xO_3$ ($x = 0.05, 0.10$). The hollow markers show corresponding calculated values. The straight lines represent 100% (dotted), 30% (black), and 15% (red) contribution of Nb $4d^1$ electron concentration in E_p.

The controllable characteristics of this unconventional plasmonic oscillation in the Nb-substituted EBTOs have high prospects in the technological applications, especially as plasmonic materials in the IR region. This set of prospective oxides can provide a choice to customize the materials properties suitable for device fabrications by tuning the plasmon energy in the IR to mid-IR range as well as by tuning the Mott transitions and, hence, the band gap in the IR-visible range (1−3 eV). The low-loss window in the IR-visible range may provide some critical advantages in using these perovskites for transformation optics.

V. CONCLUSIONS

In summary, we report the formation of a quasilocal low-energy (IR-range) plasmon in Nb-substituted EBTOs, $Eu_{0.30}Ba_{0.70}Ti_{(1-x)}Nb_xO_3$ ($0 \leqslant x \leqslant 0.10$) with a simultaneous occurrence of insulator-metal transition for $x = 0.10$. The quasilocal plasmons are originated from f-d hybridizations and can be precisely controlled by the Nb substitution at room temperature. Our paper underlines a prospect of tailoring the dielectric properties in Nb-substituted EBTO perovskites suitable for applications in plasmonics, transformation optics, biosensing, etc., in IR- to visible-energy regions.

ACKNOWLEDGMENTS

This work is supported by the Ministry of Education (MOE) (Grants No. MOE2015-T2-2-065, No. MOE2015-T2-1-099, No. MOE2016-T2-1-054, and No. MOE2017-T2-1-135) Singapore National Research Foundation under its Competitive Research Funding (Grants No. NRF-CRP 8-2011-06 and No. NRF-CRP15-2015-01) and FRC (Grants

No. R-144-000-379-114 and No. R-144-000-368-112), 2015 PHC Merlion project, and NUS Core Support (Grant No. C-380-003-003-001). R.M. and A.R. acknowledge MOE Grant No. MOE2015-T2-2-147. R.M. also acknowledges funding (Grant No. MOE-2014-T2-118) received from the MOE. The authors would like to acknowledge the Singapore Synchrotron Light Source (SSLS) for providing the facility necessary for conducting the research. The SSLS is a National Research Infrastructure under the National Research Foundation Singapore.

[1] J. B. Pendry, A. J. Holden, W. J. Stewart, and I. Youngs, Phys. Rev. Lett. **76**, 4773 (1996).

[2] A. Sobhani, M. W. Knight, Y. Wang, B. Zheng, N. S. King, L. V. Brown, Z. Fang, P. Nordlander, and N. J. Halas, Nat. Commun. **4**, 1643 (2013).

[3] H. Hu, X. Yang, F. Zhai, D. Hu, R. Liu, K. Liu, Z. Sun, and Q. Dai, Nat. Commun. **7**, 12334 (2016).

[4] R. W. Johns, H. A. Bechtel, E. L. Runnerstrom, A. Agrawal, S. D. Lounis, and D. J. Milliron, Nat. Commun. **7**, 11583 (2016).

[5] F. D'Apuzzo, A. R. Piacenti, F. Giorgianni, M. Autore, M. C. Guidi, A. Marcelli, U. Schade, Y. Ito, M. Chen, and S. Lupi, Nat. Commun. **8**, 14885 (2017).

[6] R. Adato, A. A. Yanik, J. J. Amsden, D. L. Kaplan, F. G. Omenetto, M. K. Hong, S. Erramilli, and H. Altug, Proc. Natl. Acad. Sci. USA **106**, 19227 (2009).

[7] S. Kawata, Y. Inouye, and P. Verma, Nat. Photonics **3**, 388 (2009).

[8] T. S. Bui, T. D. Dao, L. H. Dang, L. D. Vu, A. Ohi, T. Nabatame, Y. Lee, T. Nagao, and C. V. Hoang, Sci. Rep. **6**, 32123 (2016).

[9] A. Ameen, L. P. Hackett, S. Seo, F. K. Dar, M. R. Gartia, L. L. Goddard, and G. L. Liu, Adv. Opt. Mater. **5**, 1601051 (2017).

[10] Y. Tian and T. Tatsuma, J. Am. Chem. Soc. **127**, 7632 (2005).

[11] V. E. Ferry, L. A. Sweatlock, D. Pacifici, and H. A. Atwater, Nano Lett. **8**, 4391 (2008).

[12] R. A. Pala, J. White, E. Barnard, J. Liu, and M. L. Brongersma, Adv. Mater. **21**, 3504 (2009).

[13] Y. Nishijima, K. Ueno, Y. Yokota, K. Murakoshi, and H. Misawa, J. Phys. Chem. Lett. **1**, 2031 (2010).

[14] J. B. Pendry, D. Schurig, and D. R. Smith, Science **312**, 1780 (2006).

[15] A. V. Kildishev and V. M. Shalaev, Opt. Lett. **33**, 43 (2008).

[16] V. M. Shalaev, Science **322**, 384 (2008).

[17] C. V. Hoang, K. Hayashi, Y. Ito, N. Gorai, G. Allison, X. Shi, Q. Sun, Z. Cheng, K. Ueno, K. Goda, and H. Misawa, Nat. Commun. **8**, 771 (2017).

[18] G. V. Naik, J. Kim, and A. Boltasseva, Opt. Mater. Express **1**, 1090 (2011).

[19] G. V. Naik, V. M. Shalaev, and A. Boltasseva, Adv. Mater. **25**, 3264 (2013).

[20] K. Rubi and R. Mahendiran, arXiv:1802.06337.

[21] X. Yin, M. A. Majidi, X. Chi, P. Ren, L. You, N. Palina, X. Yu, C. Diao, D. Schmidt, B. Wang, P. Yang, M. B. H. Breese, J. Wang, and A. Rusydi, NPG Asia Mater. **7**, e196 (2015).

[22] X. Yu, O. Wilhelmi, H. O. Moser, S. V. Vidyaraj, X. Gao, A. T. S. Wee, T. Nyunt, H. Qian, and H. Zheng, J. Electron. Spectrosc. Relat. Phenom. **144**, 1031 (2005).

[23] J. E. Mark, *Physics and Properties of Polymers Handbook* (American Institute of Physics, New York, 1997).

[24] J. L. M. van Mechelen, D. van der Marel, C. Grimaldi, A. B. Kuzmenko, N. P. Armitage, N. Reyren, H. Hagemann, and I. I. Mazin, Phys. Rev. Lett. **100**, 226403 (2008).

[25] D. Khomskii, *Transition Metal Compounds* (Cambridge University, Cambridge, England, 2014).

[26] S. Zollner, A. A. Demkov, R. Liu, P. L. Fejes, R. B. Gregory, P. Alluri, J. A. Curless, Z. Yu, J. Ramdani, R. Droopad, T. E. Tiwald, J. N. Hilfiker, and J. A. Woollam, J. Vac. Sci. Tech. B **18**, 2242 (2000).

[27] J. H. Lee, X. Ke, N. J. Podraza, L. F. Kourkoutis, T. Heeg, M. Roeckerath, J. W. Freeland, C. J. Fennie, J. Schubert, D. A. Muller, P. Schiffer, and D. G. Schlom, Appl. Phys. Lett. **94**, 212509 (2009).

[28] T. C. Asmara, D. Wan, Y. Zhao, M. A. Majidi, C. T. Nelson, M. C. Scott, Y. Cai, B. Yan, D. Schmidt, M. Yang, T. Zhu, P. E. Trevisanutto, M. R. Motapothula, Y. P. Feng, M. B. H. Breese, M. Sherburne, M. Asta, A. Minor, T. Venkatesan, and A. Rusydi, Nat. Commun. **8**, 15271 (2017).

[29] Y. Cao, X. Liu, M. Kareev, D. Choudhury, S. Middey, D. Meyers, J. W. Kim, P. J. Ryan, J. W. Freeland, and J. Chakhalian, Nat. Commun. **7**, 10418 (2016).

[30] C. Chen, J. Avila, E. Frantzeskakis, A. Levy, and M. C. Asensio, Nat. Commun. **6**, 8585 (2015).

[31] A. E. Bocquet, T. Mizokawa, T. Saitoh, H. Namatame, and A. Fujimori, Phys. Rev. B **46**, 3771 (1992).

[32] M. Nakayama, M. Xue, W. An, P. Liu, and M. G. White, J. Phys. Chem. C **119**, 14756 (2015).

[33] W. Li, R. Zhao, L. Wang, R. Tang, Y. Zhu, J. H. Lee, H. Cao, T. Cai, H. Guo, C. Wang, L. Ling, L. Pi, K. Jin, Y. Zhang, H. Wang, Y. Wang, S. Ju, and H. Yang, Sci. Rep. **3**, 2618 (2013).

[34] Y. Shao, Ph.D. thesis, McMaster University, 2009.

[35] H. Akamatsu, Y. Kumagai, F. Oba, K. Fujita, H. Murakami, K. Tanaka, and I. Tanaka, Phys. Rev. B **83**, 214421 (2011).

[36] C. Baeumer, C. Schmitz, A. Marchewka, D. N. Mueller, R. Valenta, J. Hackl, N. Raab, S. P. Rogers, M. I. Khan, S. Nemsak, M. Shim, S. Menzel, C. M. Schneider, R. Waser, and R. Dittmann, Nat. Commun. **7**, 12398 (2016).

[37] E. Stoyanov, F. Langenhorst, and G. Steinle-Neumann, Am. Mineral. **92**, 577 (2007).

[38] Y. Shao, C. Maunders, D. Rossouw, T. Kolodiazhnyi, and G. A. Botton, Ultramicroscopy **110**, 1014 (2010).

[39] K. Jiang, R. Zhao, P. Zhang, Q. Deng, J. Zhang, W. Li, Z. Hu, H. Yang, and J. Chu, Phys. Chem. Chem. Phys. **17**, 31618 (2015).

[40] X. Y. Zhang, M. J. Rozenberg, and G. Kotliar, Phys. Rev. Lett. **70**, 1666 (1993).

[41] J. L. M. van Mechelen, Ph.D. thesis, Université de Genéve, 2010.